Electrochimica Acta 250 (2017) 91–98

Contents lists available at ScienceDirect

Electrochimica Acta

journal homepage: www.elsevier.com/locate/electacta

Graphene/graphene nanoribbon aerogels as tunable three-dimensional framework for efficient hydrogen evolution reaction

Zhen Sun, Wei Fan*, Tianxi Liu*

State Key Laboratory for Modification of Chemical Fibers and Polymer Materials, College of Materials Science and Engineering, Donghua University, 2999 North Renmin Road, Shanghai 201620, PR China

ARTICLE INFO

Article history:
Received 24 May 2017
Received in revised form 20 July 2017
Accepted 2 August 2017
Available online 3 August 2017

Keywords:
graphene
graphene nanoribbon
aerogel
MoS_2
hydrogen evolution reaction

ABSTRACT

Carbon-based materials have emerged as the promising templates of electrocatalysts for hydrogen evolution reaction (HER). In order to enhance the HER activity, the structure of carbon-based materials needs to be carefully engineered to maximize the exposure of active sites, improve the electrical conductivity and shorten the ion diffusion pathway of catalysts. In this work, high-performance electrocatalysts for HER have been constructed based on the graphene/graphene nanoribbon (GGNR) aerogels. In the GGNR aerogels, graphene nanosheets act as the main building blocks of the monolithic aerogels, while large amounts of graphene nanoribbons tightly bridge different graphene nanosheets, which allows intrinsically good electrical contact with electroactive materials. Moreover, the three-dimensional porous framework with large surface-to-volume ratio can be tuned by adjusting the amount of graphene nanoribbons, which guarantees the ultrafast and sufficient mass transfer in the catalytic process. All the above factors make GGNR aerogels ideal templates for immobilization of MoS_2 nanosheets, a typical noble metal-free hydrogen evolution catalyst. The optimal GGNR@MoS_2 hybrid exhibits excellent HER performance, with a low onset potential of −105 mV, a small Tafel slope of 49 mV per decade and a large current density (10.0 mA cm^{-2} at η = 183 mV), making them promising and highly efficient electrocatalyst for hydrogen evolution reaction.

1. Introduction

The overuse and strong dependence of fossil fuels are intensifying global environmental pollution and the energy crisis [1–3]. Hydrogen, a clean and renewable fuel, is universally recognized as a promising candidate as a future energy carrier. However, the effective production and safe storage of hydrogen are still the key issues preventing hydrogen from becoming the energy carrier [4]. Water splitting has attracted growing attention for the relatively mature technology and low cost [5]. Highly active hydrogen evolution catalysts are required to make the water splitting process more energy-efficient and economical. Although Pt and Pt-based materials are the best hydrogen evolution reaction (HER) catalysts [6], the high cost and earth-limited storage restrict their wide applications [7]. Thus, replacement of this expensive and precious metal with cost-effective and earth-abundant materials is a matter of utmost urgency [8].

Transition-metal dichalcogenides (TMDs), such as MoS_2, $MoSe_2$ [9–12], CoS_2 [13–16], WSe_2 [17,18], have been recognized as promising HER catalysts due to their tunable band structure and intrinsic electrochemical activities. Among all these TMDs, molybdenum disulfide (MoS_2) has received tremendous attention owing to the high activity and earth-abundant composition, inducing the rapid development of various kinds of MoS_2-based HER electrocatalysts [19–23]. Both experimental and theoretical calculations confirm that the HER activity of MoS_2 correlates with the number of catalytically active unsaturated S-edge sites [17,24]. Hence, designing MoS_2 nanostructures to expose more active edges is an effective strategy to obtain an efficient MoS_2-based HER electrocatalyst. In this regard, edge-oriented MoS_2 nanoporous films [25], defect-rich MoS_2 [26], and edge-exposed MoS_2 nano-assemblies [27] have been explored. Besides designing MoS_2 nanostructures, another approach to improve the HER activity is to enhance the electrical conductivity of electrocatalysts. Therefore, constructing hybrids of MoS_2 with highly conductive templates could not only facilitate the electronic transfer through the electrocatalyst but also confine MoS_2 to grow into nanostructures, thus fully exerting the excellent intrinsic properties of electrochemically active materials.

* Corresponding authors.
E-mail addresses: weifan@dhu.edu.cn (W. Fan), txliu@dhu.edu.cn, txliu@fudan.edu.cn (T. Liu).

http://dx.doi.org/10.1016/j.electacta.2017.08.009
0013-4686/

Carbon materials have been recognized as ideal templates to enhance the conductivity of the MoS_2-based electrocatalysts, due to their good conductivity and universal abundance [28–33]. For example, MoS_2 has been synthesized on graphene and the composite exhibits high activity and durability toward HER [31]. In the system, the conducting graphene provides the internal electron transport channels between the MoS_2 nanosheets and the electrodes. However, the two-dimensional graphene sheets may inevitably restack during the reduction process, hindering the full exposure of the electroactive area. To make the full utilization of graphene and acquire high-performance catalysts for HER, a practical and feasible approach is to assemble graphene into three-dimensional (3D) aerogels [34–36]. Zhao et al. successfully synthesized 3D graphene-aerogel-supported MoS_2 nanosheets, which were demonstrated as highly active and stable catalysts for the hydrogen evolution reaction [37]. The result did show that the unique 3D porous architecture and large active surface areas lead to superior HER activity with low overpotential and high catalytic current density. However, the 3D porous structure of graphene aerogels is uncontrollable and partial aggregation of graphene compromises its performance due to the existence of boundaries in the self-assembly process of 3D networks. Therefore, assembling graphene into macroscopic bulk materials with desired structures and performances still remains a great challenge. One of the promising solutions is to fabricate graphene-based hybrid aerogels, in which other nanostructures or functional materials are introduced into the graphene framework to reinforce the network structure and improve performance [38–40]. Graphene nanoribbons (GNRs) are thin strips of graphene made by longitudinally unzipping carbon nanotubes (CNTs), which not only retain the unique characteristics of graphene sheets, but also possess special properties, such as a high length-to-width ratio, straight edges, and ideal surface regularity with few defects on the basal plane [41,42]. Therefore, assembling GNRs with graphene into hybrid aerogels can adjust the network structure to improve the electrocatalytic performance for hydrogen evolution reaction.

In this work, graphene/graphene nanoribbon (GGNR) hybrid aerogels, fabricated by facile freeze-drying method, have been employed as a highly conductive 3D framework for the anchoring of few-layered MoS_2. The GNR-interconnected-graphene-sheet nanostructure can improve the electrical conductivity of the whole hybrid catalyst, thus facilitating the rapid transfer of electrons. Besides, the 3D porous structure of GGNR aerogel can be adjusted by controlling the ratio of graphene to GNRs, which can optimize the ion diffusion pathway of the catalysts. Furthermore, planar graphene sheets and nanoribbons allow the intimate growth of highly dispersed and perpendicularly oriented MoS_2 nanosheets, thus maximizing the exposure of active sites for HER. Benefiting from the unique hierarchical structures, the GGNR@MoS_2 hybrid aerogel has been demonstrated to be an excellent electrocatalyst for HER, with a low onset potential of −105 mV, a small Tafel slope of 49 mV per decade as well as a large current density (10.0 mA cm^{-2} at η = 183 mV) in acid media. Moreover, apart from fabricating an efficient HER catalyst, this work also provides a practical strategy for designing 3D framework of graphene sheets interconnected nanoribbons, which has great potential for applications in extended energy-related areas.

2. Experimental section

2.1. Reagents

Multi-walled carbon nanotubes (MWCNTs) (diameter: 30–50 nm) were obtained from Chengdu Organic Chemicals Co. Ltd., synthesized by the chemical vapor deposition method. H_2SO_4 (95–98%), H_3PO_4 (85%), H_2O_2 (30%), *N*,*N*-dimethylformamide (DMF, ≥99.5%), ethanol, potassium permanganate ($KMnO_4$), and 37% HCl were commercially purchased from Shanghai Chemical Reagent Company. Natural graphite powder (325 mesh) was purchased from Alfa-Aesar (Ward Hill, MA) and used without any other treatments. Ammonium tetrathiomolybdate ($(NH_4)_2MoS_4$) was supplied by J&K Chemical. Deionized (DI) water was used throughout all the experiments.

2.2. Preparation of GO_xGONR_y aerogels

Graphene oxide (GO) was prepared from graphite according to the modified Hummers method [43], and then ultrasonicated in DI water for at least 3 h to produce the exfoliated GO suspension (4 mg mL^{-1}). Graphene oxide nanoribbons (GONR) were prepared by longitudinally unzipping MWCNTs through the solution-based oxidative process [44], and dispersed in DI water to obtain a 4 mg mL^{-1} GONR dispersion. Subsequently, dispersions of GO and GONR with different weight ratios (GO:GONR = 2:1, 1:1, 1:2) were mixed and sonicated for 5 min, followed by freeze-drying in the lyophilizer for about 24 h. Thus a series of GO_xGONR_y aerogels were obtained, denoted as GO_2GONR_1, GO_1GONR_1 and GO_1GONR_2, respectively, in which x and y correspond to the weight ratio of GO to GONR. In addition, both pure GO and GONR aerogels were prepared via the above method for comparison.

2.3. Preparation of G_xGNR_y@MoS_2 hybrids

G_xGNR_y@MoS_2 hybrids were synthesized through a facile solvothermal reaction. Briefly, a certain amount of $(NH_4)_2MoS_4$ (11 mg, 22 mg and 44 mg) was dissolved in 10 mL DMF. After that, the transparent solution was transferred into a 40 mL Teflon-lined stainless steel autoclave with a piece of GO_xGONR_y aerogel (10 mg) completely immersed into the solution. The autoclave was sealed and maintained at 180 °C for 12 h. After cooling down to room temperature, the obtained products were washed repeatedly with DI water and ethanol, and finally dried for 12 h. During the solvothermal reaction, the GO_xGONR_y aerogel was reduced to graphene/graphene nanoribbon (G_xGNR_y) simultaneously. The hybrids with different loading amounts of MoS_2 were labelled as G_xGNR_y@MoS_2-1, G_xGNR_y@MoS_2-2 and G_xGNR_y@MoS_2-3, respectively. Thus, according to the rule, the hybrid prepared from GO_1GONR_1 aerogel and 22 mg $(NH_4)_2MoS_4$ was denoted as G_1GNR_1@MoS_2-2.

For comparison, bare MoS_2 was prepared through the same procedure without addition of aerogels, and pure G_1GNR_1 aerogels were prepared by direct solvothermal reaction. G@MoS_2-2 and GNR@MoS_2-2 hybrids were synthesized by replacing G_xGNR_y aerogels with GO and GONR aerogels in the precursor, respectively. G/MoS_2-2 hybrid was fabricated by directly growing MoS_2 nanosheets on graphene sheets instead of aerogels.

2.4. Characterization of G_xGNR_y@MoS_2 hybrids

The microstructures of samples were characterized by field emission scanning electron microscopy (FESEM) (Ultra 55, Zeiss) at 5 kV acceleration voltage. Transmission electron microscopy (TEM) observations were performed by JEOL JEM 2100 TEM under 200 kV acceleration voltage. Samples for TEM observations were prepared by dropping solutions on the copper grids and drying in the air. X-ray diffraction (XRD) patterns were performed on an X'Pert Pro X-ray diffractometer with Cu Kα radiation (λ = 0.1542 nm) under a current of 40 mA and a voltage of 40 kV with 2θ range from 10° to 70°. X-ray photoelectron spectroscopy (XPS) analyses were conducted with a VG ESCALAB 220I-XL device and all XPS spectra were corrected using C1 s line at 284.5 eV. In addition, the curve fitting and background subtraction were accomplished using XPS

PEAK41 software. The specific surface area of GO aerogels and GO_1GONR_1 aerogels were characterized with a belsorp-max surface area detecting instrument (Tristar3000) by N_2 physisorption at 77 K.

2.5. Electrochemical studies

2 mg of GGNR@MoS_2 hybrids was dispersed in 1 mL ethanol/DI water (volume ratio: 1/3) mixed solution along with 30 μL of 5 wt% Nafion solution, followed by sonication for 30 min to get a homogeneous slurry. Then 10 μL of the slurry was dropped onto a glassy carbon electrode (GCE) with 3 mm in diameter and dried at room temperature. For comparison, pure G_1GNR_1 aerogel, MoS_2 and G/MoS_2 modified GCEs were also prepared in the same way.

All the electrochemical tests were performed with a standard three-electrode setup using a CHI 660D electrochemical workstation (Shanghai Chenhua Instrument Co., China) at room temperature, where the hybrids modified GCE was applied as the working electrode, a graphite rod as the counter electrode and a saturated calomel electrode (SCE) as the reference electrode. Linear sweep voltammetry (LSV) was measured with a scan rate of 2 mV s^{-1} in nitrogen purged 0.5 M H_2SO_4 solution. AC impedance measurements were carried out with frequencies ranging from 0.01 Hz to 100 kHz with an amplitude of 5 mV. The electrocatalytic stability of products was evaluated by testing current-time responses at −200 mV for 30000 s. All of the potentials were calibrated to a reversible hydrogen electrode (RHE).

3. Results and Discussion

3.1. Morphology and structure of G_xGNR_y@MoS_2 hybrids

The fabrication process of G_xGNR_y@MoS_2 hybrids is schematically illustrated in Fig. 1. GO sheets were obtained by the modified Hummers method and clearly showed a sheet-like structure (Fig. S1). GONRs were prepared through the solution-based chemical unzipping of MWCNTs, resulting in nanoribbons with width of 100–200 nm (Fig. S2). The two suspensions with desired concentrations were mixed together and subjected to freeze-drying to form a porous GO_xGONR_y aerogel (digital photo shown in Fig. S3). These GO_xGONR_y aerogels are constructed by GONR interconnected GO nanosheets via hydrogen bond and π-π interactions in 3D configuration, resulting in a highly porous network. The structure and morphology of the as-prepared aerogels were investigated via FESEM images (Fig. 2). FESEM images clearly reveal that all the prepared aerogels show an interconnected, porous structure with hierarchical pores ranging from hundreds of nanometers to tens of micrometers. A close view of the pore walls reveals that the two terminals of GONRs attach mostly on different graphene sheets separately (Fig. 2d). These GONRs maintain the original ribbon-like morphology with lengths of tens of micrometers and width of about hundreds of nanometers, and most of them distribute individually among the graphene sheets without forming aggregations, indicating homogeneous distribution of GONR and GO sheets. These GONRs bridge individual GO sheets by forming a nanoribbon-interconnected-nanosheet structure, making the open pore walls and even the whole aerogel stronger, thus ensuring that the interconnected porous construction remains without collapse. Besides, compared with the GO aerogels (Fig. S4a,b) and GONR aerogels (Fig. S4c,d), the GO_xGONR_y aerogel possesses more homogeneous pore distribution, attributing to its nanoribbon-interconnected-nanosheet structure. As indicated by the nitrogen adsorption/desorption isotherms shown in Fig. S5, the specific surface area of GO_1GONR_1 aerogels is 256 $m^2 g^{-1}$, which is relatively larger than that of GO aerogels (148 $m^2 g^{-1}$). The average macropore size varies with different GONR contents, with an optimized pore size of about 10 μm for GO_1GONR_1 (Fig. 2c), indicating that tunable graphene aerogels can be obtained by adjusting the initial different weight ratios of GO and GONR. The decrease of the size of the macropore can also increase the space utilization, which can provide more surface areas for in-situ growth of MoS_2 nanosheets with the same volume.

Afterwards, MoS_2 nanosheets were grown onto GO_xGONR_y aerogel via a solvothermal reaction, and GO_xGONR_y aerogels were reduced simultaneously, resulting in G_xGNR_y@MoS_2 hybrids. The FESEM images of G_1GNR_1@MoS_2-2 are shown in Fig. 3. After solvothermal reaction, the interconnected porous structures are

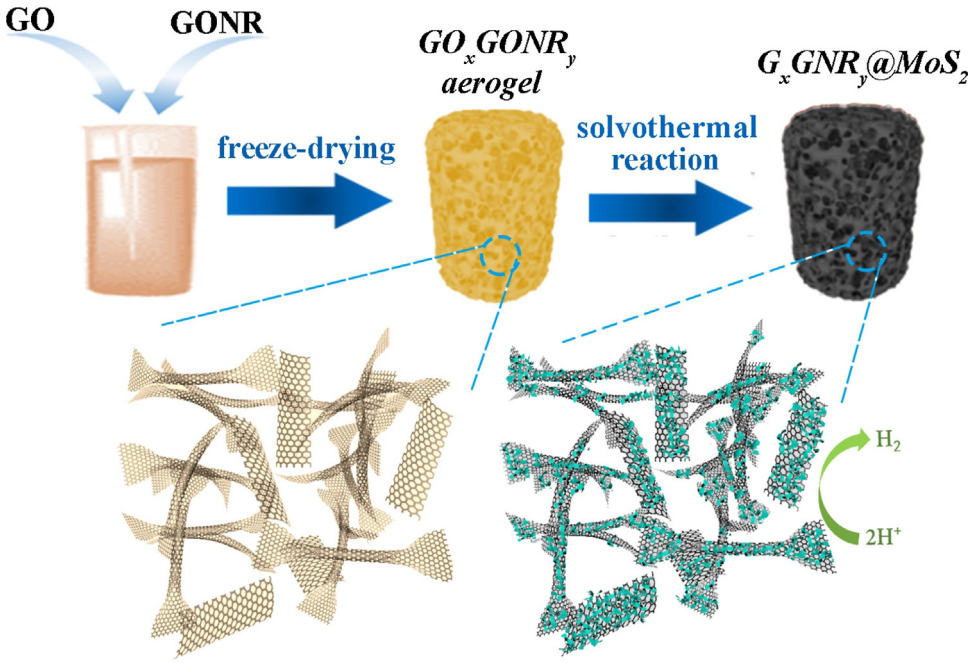

Fig 1. Schematic illustration of the preparation of G_xGNR_y@MoS_2 hybrids.

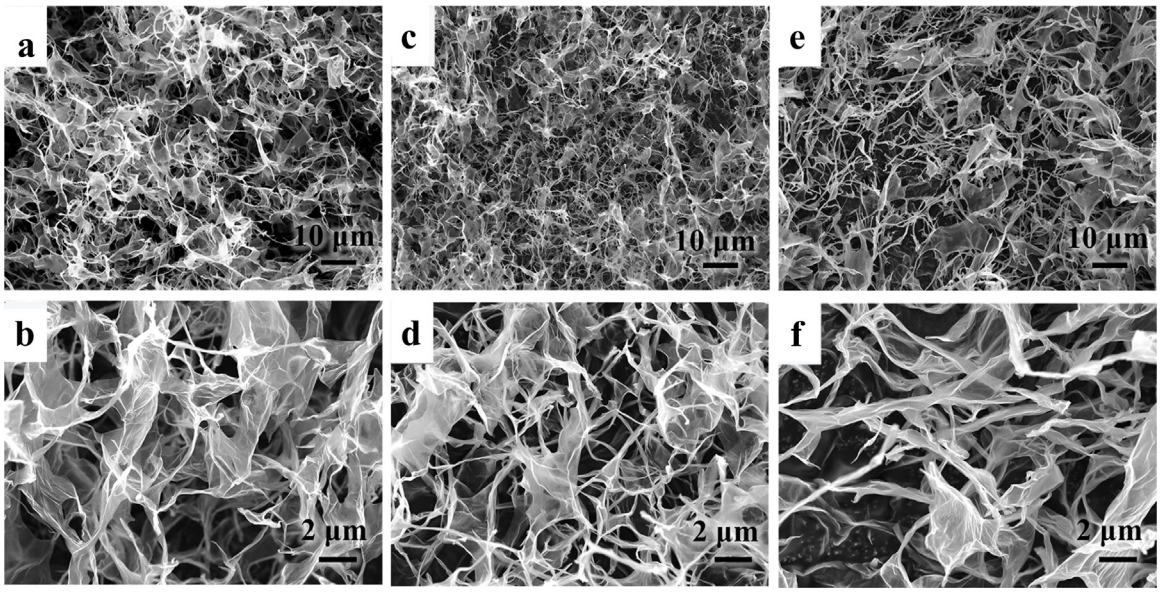

Fig. 2. FESEM images of (a, b) GO_2GONR_1, (c, d) GO_1GONR_1, and (e, f) GO_1GONR_2 aerogels at low and high magnifications, respectively.

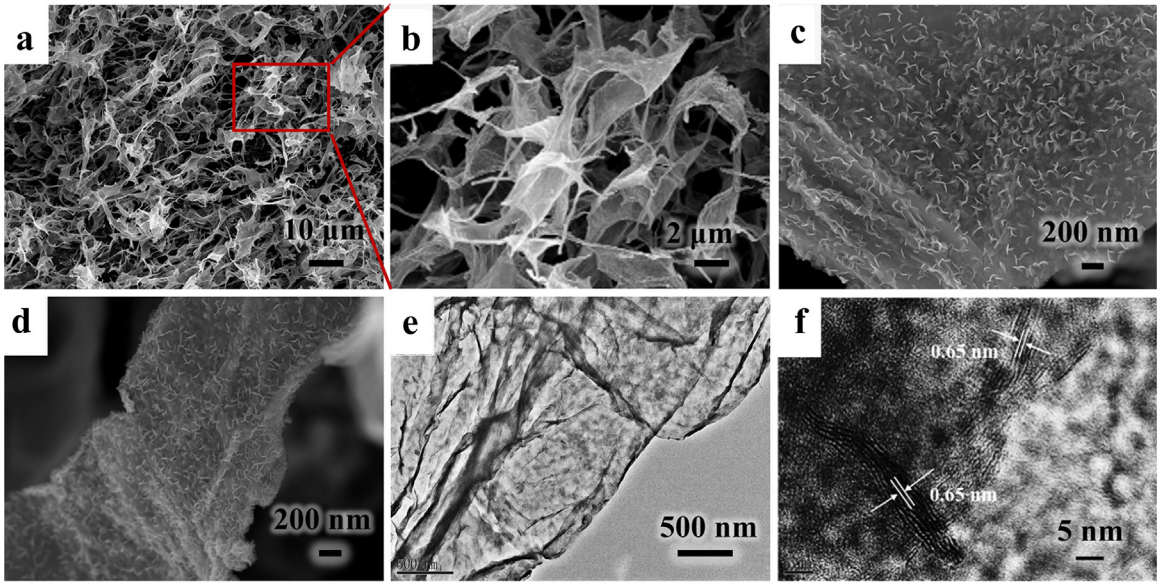

Fig. 3. FESEM images of G_1GNR_1@MoS_2-2 hybrid at (a) low and (b) high magnifications. FESEM images showing MoS_2 grows on both (c) graphene sheets and (d) GNRs in the aerogel structure. (e) TEM image and (f) high-resolution TEM image of G_1GNR_1@MoS_2-2 hybrid.

well retained for G_1GNR_1@MoS_2-2 (Fig. 3a,b), demonstrating the strong interaction between GNR and graphene nanosheets and structural integrity of G_xGNR_y aerogel. Notably, few-layered MoS_2 nanosheets are perpendicularly grown on both graphene nanosheets (Fig. 3c) and nanoribbons (Fig. 3d) homogeneously. TEM image of G_1GNR_1@MoS_2-2 hybrid (Fig. 3e) reveals that vertically oriented MoS_2 nanosheets are homogeneously anchored onto the two-dimensional graphene nanosheets, which is in good agreement with the FESEM images. From the HRTEM image in Fig. 3f, 3–8 layers of MoS_2 nanosheets can be clearly observed, and the interlayer spacing of MoS_2 nanosheets is about 0.65 nm, which is slightly larger than the layer-to-layer spacing of 0.61 nm in bulk MoS_2. In addition, it is worth noting that the crystal fringes are discontinuous, which can be attributed to the existence of rich defects.

XRD patterns and XPS spectra were further investigated to confirm the composition of the hybrids. Fig. 4a shows the XRD patterns of G_1GNR_1 aerogel, MoS_2 and G_1GNR_1@MoS_2-2 hybrids. Different from GO and GONR showing sharp diffraction peaks at $2\theta = 9°–11°$ (Fig. S6), G_1GNR_1 aerogel displays a board peak ranging from 20° to 30°, which is assigned to (002) plane of chemically reduced graphene, indicating the reduction of GO and GONR after the solvothermal reaction. The pure MoS_2 displays diffraction peaks at $2\theta = 14.2°$, 33.8°, and 59.3°, which can be well indexed to (002), (100), and (110) planes of the hexagonal MoS_2 phase (JCPDS: 00-037-1492), respectively. The XRD pattern of G_1GNR_1@MoS_2-2 hybrid possesses the peaks of both G_1GNR_1 and MoS_2, suggesting that the MoS_2 has been grown on G_1GNR_1 aerogel successfully. Fig. 4b–d show the surface chemical states of G_1GNR_1@MoS_2 hybrid characterized by XPS. As shown in Fig. 4b, the survey scan

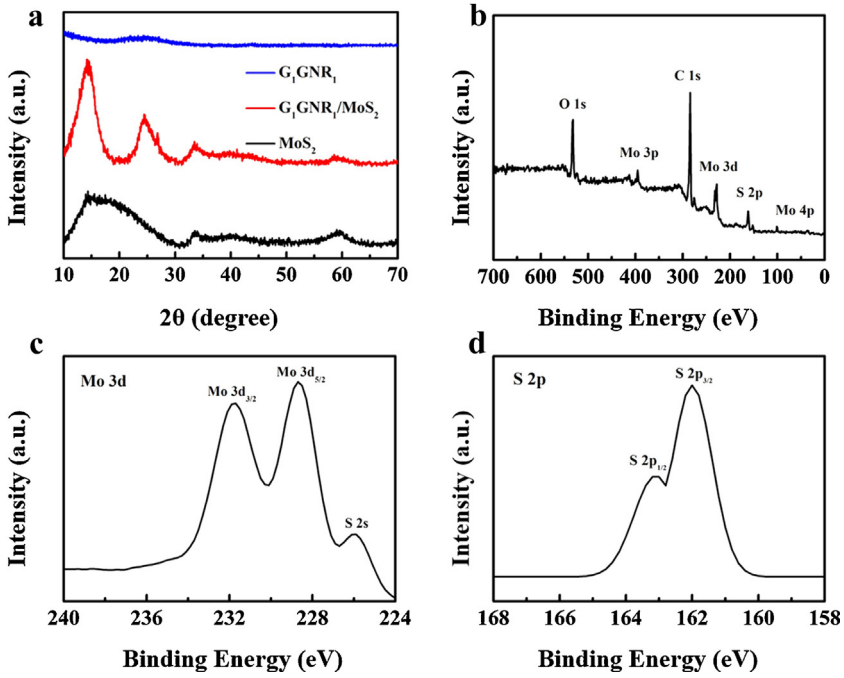

Fig. 4. (a) XRD patterns of G_1GNR_1 aerogel, MoS_2 and the G_1GNR_1@MoS_2-2 hybrid. XPS spectra of the G_1GNR_1@MoS_2-2 hybrid: (b) survey spectrum, high-resolution (c) Mo 3d, and (d) S 2p spectra.

indicates that C, Mo, S and O elements coexist in G_1GNR_1@MoS_2-2 hybrid. The high-resolution Mo 3d spectrum (Fig. 4c) exhibits two strong peaks located at 232.0 and 229.2 eV, corresponding to Mo $3d_{3/2}$ and Mo $3d_{5/2}$ orbitals, respectively, suggesting that Mo in G_1GNR_1@MoS_2-2 hybrid is in Mo (IV) state. In the high-resolution S 2p spectrum (Fig. 4d), the peaks at 163 and 162 eV are observed, referring to S $2p_{1/2}$ and S $2p_{3/2}$ orbitals of divalent sulfide ions (S^{2-}), respectively. All the results further demonstrate the successful preparation of G_1GNR_1@MoS_2-2 hybrid.

3.2. HER electrocatalytic activity of G_xGNR_y@MoS_2 hybrids

The electrocatalytic activities of G_xGNR_y@MoS_2 hybrids for HER were investigated in acid media of 0.5 M H_2SO_4 solution using a typical three-electrode setup at a scan rate of 2 mV s^{-1}. Fig. 5 shows the HER catalytic performance of a series of G_xGNR_y@MoS_2-2 hybrids. Among the G_xGNR_y@MoS_2-2 hybrids, G_1GNR_1@MoS_2-2 hybrid exhibits the optimal HER catalytic performance with the

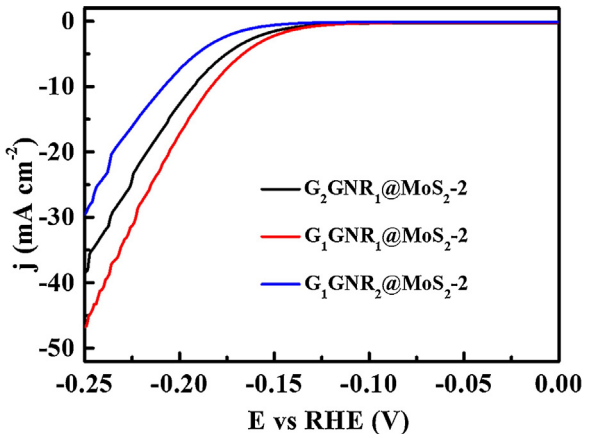

Fig. 5. LSV polarization curves of G_2GNR_1@MoS_2-2, G_1GNR_1@MoS_2-2 and G_1GNR_2@MoS_2-2 modified GCE in N_2-purged 0.5 M H_2SO_4 solution. Scan rate: 2 mV s^{-1}.

onset potential of −105 mV vs RHE and significant hydrogen evolution (j = 10 mA cm^{-2}) observed at a voltage of −183 mV, with the other two curves more or less negatively shifted. The difference of electrocatalytic activity between these hybrids with different ratios of graphene and GNR can be explained by their porous structure. The G_1GNR_1 aerogel shows more homogeneous pore size distribution, attributing to its nanoribbon-interconnected-nanosheet structure, which can provide more surface areas for in-situ growth of MoS_2 nanosheets with the same volume.

Meanwhile, in order to uncover the interplay between the loading amount of MoS_2 and the electrocatalytic activity, G_1GNR_1@MoS_2-1, G_1GNR_1@MoS_2-2, and G_1GNR_1@MoS_2-3 were all measured for the HER performance in acidic solution and the corresponding LSV curves are presented in Fig. 6a. G_1GNR_1@MoS_2-2 presents an optimal HER catalytic activity since the current density increases most rapidly with the lowest onset potential than that of the other two counterparts. MoS_2 nanoparticles are densely distributed on the surface of G_1GNR_1@MoS_2-2 (Fig. 6c), providing much more abundant active catalytic sites than G_1GNR_1@MoS_2-1 (Fig. 6b). In contrast, an overloaded amount of MoS_2 nanosheets is overspread on the G_1GNR_1 template in the G_1GNR_1@MoS_2-3 hybrid (Fig. 6d), resulting in the aggregation of MoS_2 nanosheets, which reduces the exposure of active edge sites to electrolyte and the fast transfer of the electron from the substrate to the active sites. All these prove that proper loading of MoS_2 nanosheets on aerogel surface could facilitate the full utilization of active edge sites of catalyst and rapid electron transport simultaneously.

Further comparison of HER performance among pure G_1GNR_1, MoS_2, G@MoS_2-2, G/MoS_2-2, GNR@MoS_2-2, G_1GNR_1@MoS_2-2 hybrids and commercially available Pt can reveal the vital role of G_xGNR_y aerogel to the electrochemical catalysis. The corresponding LSV curves are shown in Fig. 7a. It is clear that the bare GCE is electrochemical inert (Fig. S7). The Pt catalyst exhibits superb HER activity, with a near zero overpotential and a large current density, while pure G_1GNR_1 displays no catalytic performance. Although pure MoS_2 agglomerates exhibit unnegligible electrocatalytical performance, the onset potential and current

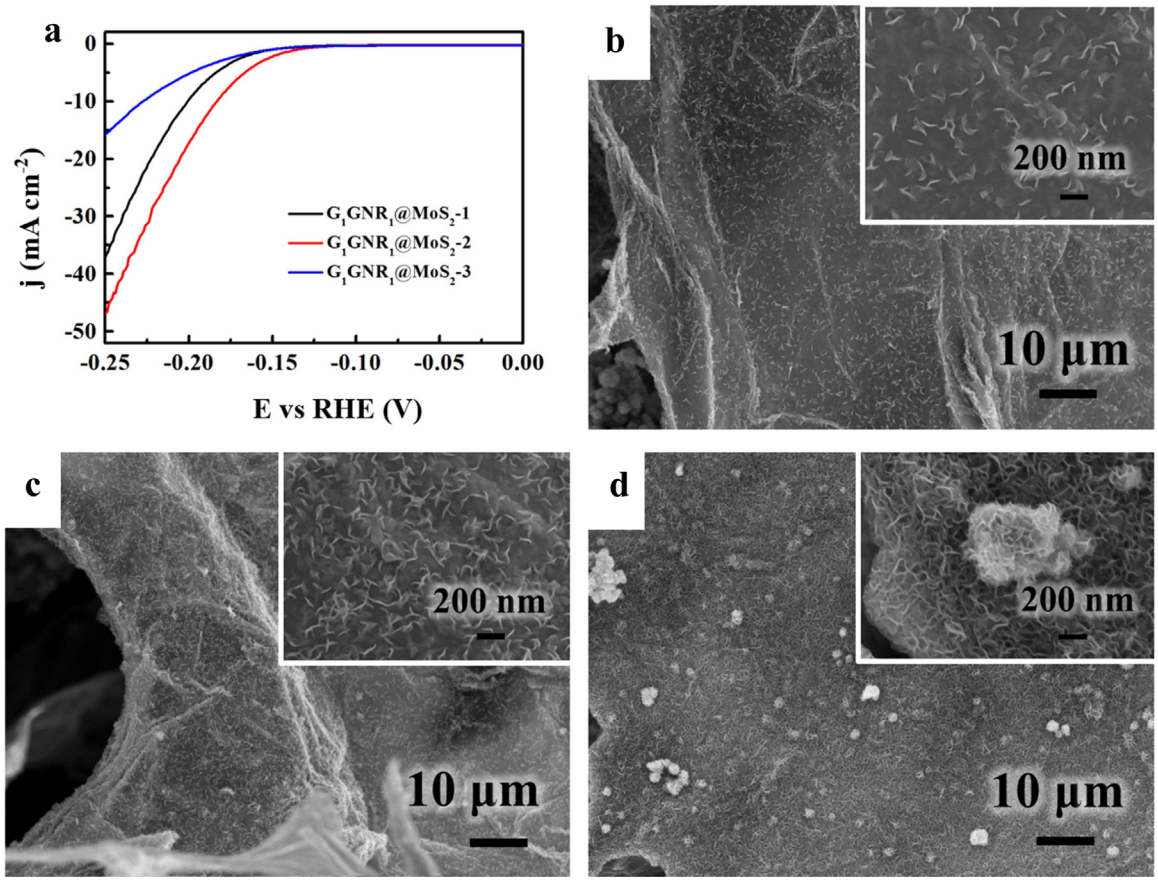

Fig. 6. (a) LSV polarization curves of G_1GNR_1@MoS_2-1, G_1GNR_1@MoS_2-2 and G_1GNR_1@MoS_2-3 modified GCE in N_2-purged 0.5 M H_2SO_4 solution. Scan rate: 2 mV s^{-1}. FESEM images of (b) G_1GNR_1@MoS_2-1, (c) G_1GNR_1@MoS_2-2, (d) G_1GNR_1@MoS_2-3 hybrids. The inset images show the corresponding close-up view at high magnifications.

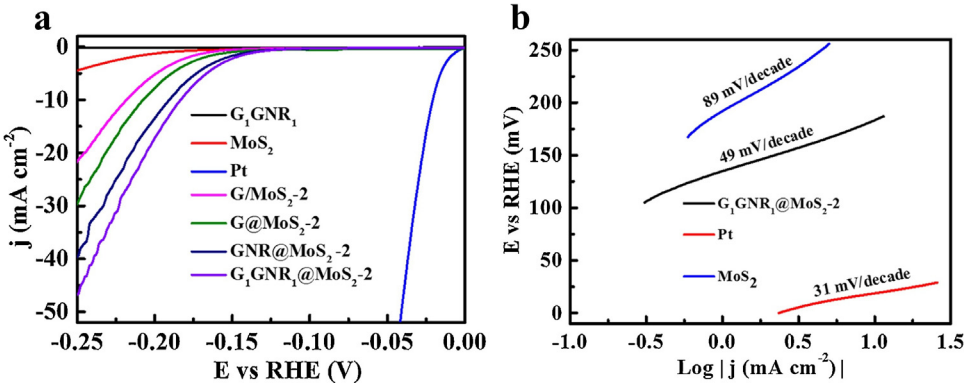

Fig. 7. (a) LSV polarization curves of different materials modified GCE in N_2-purged 0.5 M H_2SO_4 solution. Scan rate: 2 mV s^{-1}. (b) Tafel plots for the pure MoS_2 nanosheets, G_1GNR_1@MoS_2-2 and Pt modified GCE.

density are far inferior to those of the G@MoS_2-2, GNR@MoS_2-2, G_1GNR_1@MoS_2-2 hybrids, which results from the lack of an efficient template with high conductivity and high surface area to hold back its serious aggregation (Fig. S8). It is also worth noting that G@MoS_2-2 with graphene aerogel as substrate shows better electrocatalytic activity than the G/MoS_2-2 (prepared by growing MoS_2 on graphene sheets), as the aerogel structure prevents the graphene nanosheets from restacking and provides 3D open structure for fast ion diffusion. Compared with pure graphene or GNR aerogel substrate, the optimal catalytic performance of the G_1GNR_1@MoS_2-2 hybrid can be credited to the following three aspects: (1) The nanoribbon-interconnected-nanosheet structure could improve the electrical conductivity of whole hybrid catalyst, thus facilitating the rapid transfer of electrons. (2) The optimized 3D porous structure of G_1GNR_1 aerogel can facilitate the ion diffusion during the catalytic process. (3) Highly dispersed MoS_2 nanosheets can be perpendicularly grown on both graphene sheets and nanoribbons, maximizing the exposure of active sites for HER.

The Tafel slope is an inherent property of the catalyst and determined by the rate-limiting step of the HER. The corresponding Tafel plots are shown in Fig. 7b. For G_1GNR_1@MoS_2-2 measured in 0.5 M H_2SO_4, the Tafel slope is calculated to be 49 mV $decade^{-1}$,

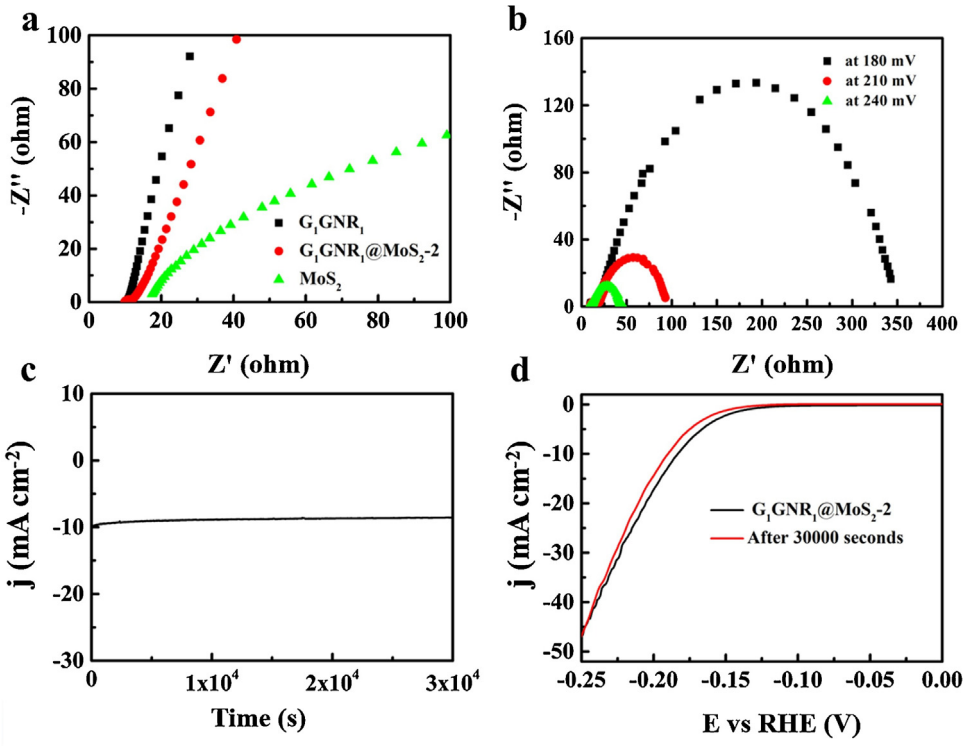

Fig. 8. (a) Nyquist plots for the G_1GNR_1, MoS_2 and G_1GNR_1@MoS_2-2 hybrid at the open-circuit voltage. (b) Nyquist plots for G_1GNR_1@MoS_2-2 hybrid at different overpotentials. (c) Time dependence of current density under static overpotential of 200 mV. (d) Comparison of LSV polarization curves for G_1GNR_1@MoS_2-2 hybrid before and after cycling test.

lower than that of pure MoS_2 (89 mV decade^{-1}), suggesting prominent contribution to the fast HER electrochemical reaction. The small Tafel slope of the G_1GNR_1@MoS_2-2 is advantageous for practical applications, since it will result in a faster increment of HER rate with increasing overpotential. The Tafel slope of 49 mV decade^{-1} for G_1GNR_1@MoS_2-2 indicates that HER activity occurs through a Volmer-Heyrovsky mechanism with Heyrovsky reaction as the rate-limiting step.

In order to evaluate the interface reactions and catalytic kinetics in the HER process, electrochemical impedance spectroscopy (EIS) measurements were carried out in a frequency range from 100 kHz to 0.01 Hz. Fig. 8a shows the Nyquist plots for the G_1GNR_1, MoS_2 and G_1GNR_1@MoS_2-2 hybrid at the open-circuit voltage. As is well known, the larger slope represents the better electrical conductivity of the electrocatalysts, while the solution resistance (R_s), deduced from the intersection of the real axis in the range of the high frequency region, can reflect the interface reactions. The more vertical curve and the reduced R_s of G_1GNR_1@MoS_2-2 reveal the better electrical conductivity and improved the electron transfer between the electrolyte ions and hybrid material compared with pure MoS_2. R_{ct} represents the charge transfer resistance, which corresponds to the semicircle of Nyquist plots. The R_{ct} decreases with the increase of overpotential (Fig. 8b), which reveals that more efficient hydrogen generation takes place, along with more rapid electron transfer.

Another critical criterion for evaluating hydrogen production of non-noble-metal catalysts is the long-term stability in working environments. Fig. 8c shows the continuous HER at static overpotential with a long period of 30000 seconds. When an overpotential of 200 mV was applied, a continuous HER process occurred to generate H_2. Obviously, the current density exhibits only slight degradation even after a long period of 30000 seconds, which may result from the residuary bubbles on the surface of the electrode hampering the electron transfer between the electrolyte ions and the catalyst. Fig. 8d displays the comparison of LSV polarization curves measured before and after 30000 s continuous HER. The negligible difference between the curves also indicates that the G_1GNR_1@MoS_2-2 is of superior stability in long-term electrochemical process.

4. Conclusions

In conclusion, high-performance electrocatalysts for HER have been constructed based on the graphene/graphene nanoribbon aerogels. In the GGNR aerogels, large amounts of the graphene nanoribbons tightly bridge between different graphene nanosheets, the main building blocks of the monolithic aerogels. The graphene nanosheet-interconnected-nanoribbon porous network with large surface-to-volume ratio guarantees the ultrafast and sufficient mass transfer and the bridging of GNRs allows intrinsically good electrical contact in the catalytic process, which make these aerogels ideal templates for immobilization of MoS_2 nanosheets. The result shows that the optimal G_xGNR_y@MoS_2 hybrid exhibits excellent HER performance, with a low onset potential of −105 mV, a small Tafel slope of 49 mV per decade and a large current density (10.0 mA cm^{-2} at η = 183 mV). This work also provides a practical strategy for designing 3D framework of graphene sheets interconnected nanoribbons, which have great potential for applications in high-performance electrocatalysts.

Acknowledgements

The authors are grateful for the financial support from the National Natural Science Foundation of China (51433001), China

Postdoctoral Science Foundation (2016M601471), Shanghai Sailing Program (17YF1400200), and the Fundamental Research Funds for the Central Universities.

Appendix A. Supplementary data

Supplementary data associated with this article can be found, in the online version, at http://dx.doi.org/10.1016/j.electacta.2017.08.009.

References

[1] T.E. Mallouk, Water electrolysis: Divide and conquer, Nature Chemistry 5 (2013) 362–363.
[2] J.K. Norskov, C.H. Christensen, Toward efficient hydrogen production at surfaces, Science 312 (2006) 1322–1323.
[3] J.A. Turner, Sustainable hydrogen production, Science 305 (2004) 972–974.
[4] X. Zou, Y. Zhang, Noble metal-free hydrogen evolution catalysts for water splitting, Chemical Society Reviews 44 (2015) 5148–5180.
[5] M. Zeng, Y.G. Li, Recent advances in heterogeneous electrocatalysts for the hydrogen evolution reaction, Journal of Materials Chemistry A 3 (2015) 14942–14962.
[6] J. Greeley, T.F. Jaramillo, J. Bonde, I. Chorkendorff, J.K. Nørskov, Computational high-throughput screening of electrocatalytic materials for hydrogen evolution, Nature Materials 5 (2006) 909–913.
[7] E. Casado-Rivera, D.J. Volpe, L. Alden, C. Lind, C. Downie, T. Vazquez-Alvarez, A. C.D. Angelo, F.J. DiSalvo, H.D. Abruna, Electrocatalytic activity of ordered intermetallic phases for fuel cell applications, Journal of the American Chemical Society 126 (2004) 4043–4049.
[8] J. Lin, Z.W. Peng, G. Wang, D. Zakhidov, E. Larios, M.J. Yacaman, J.M. Tour, Enhanced electrocatalysis for hydrogen evolution reactions from WS_2 nanoribbons, Advanced Energy Materials 4 (2014) 1301875.
[9] D.S. Kong, H.T. Wang, J.J. Cha, M. Pasta, K.J. Koski, J. Yao, Y. Cui, Synthesis of MoS_2 and $MoSe_2$ films with vertically aligned layers, Nano Letters 13 (2013) 1341–1347.
[10] X.L. Zhou, J. Jiang, T. Ding, J.J. Zhang, B.C. Pan, J. Zuo, Q. Yang, Fast colloidal synthesis of scalable Mo-rich hierarchical ultrathin $MoSe_{2-x}$ nanosheets for high-performance hydrogen evolution, Nanoscale 6 (2014) 11046–11051.
[11] L. Jia, X. Sun, Y. Jiang, S. Yu, C. Wang, A novel $MoSe_2$–reduced graphene oxide/polyimide composite film for applications in electrocatalysis and photoelectrocatalysis hydrogen evolution, Advanced Functional Materials 25 (2015) 1814–1820.
[12] S. Mao, Z. Wen, S. Ci, X. Guo, K.K. Ostrikov, J. Chen, Perpendicularly oriented $MoSe_2$/graphene nanosheets as advanced electrocatalysts for hydrogen evolution, Small 11 (2015) 414–419.
[13] M.S. Faber, M.A. Lukowski, Q. Ding, N.S. Kaiser, S. Jin, Earth-abundant metal pyrites (FeS_2, CoS_2, NiS_2, and their alloys) for highly efficient hydrogen evolution and polysulfide reduction electrocatalysis, The Journal of Physical Chemistry C 118 (2014) 21347–21356.
[14] M.S. Faber, K. Park, M. Caba'n-Acevedo, P.K. Santra, S. Jin, Earth-abundant cobalt pyrite (CoS_2) thin film on glass as a robust, high-performance counter electrode for quantum dot-sensitized solar cells, The Journal of Physical Chemistry Letters 4 (2013) 1843–1849.
[15] S. Peng, L. Li, X. Han, W. Sun, M. Srinivasan, S.G. Mhaisalkar, F. Cheng, Q. Yan, J. Chen, S. Ramakrishna, Cobalt sulfide nanosheet/graphene/carbon nanotube nanocomposites as flexible electrodes for hydrogen evolution, Angewandte Chemie International Edition 126 (2014) 12802–12807.
[16] Y. Sun, C. Liu, D.C. Grauer, J. Yano, J.R. Long, P. Yang, C.J. Chang, Electrodeposited cobalt-sulfide catalyst for electrochemical and photoelectrochemical hydrogen generation from water, Journal of the American Chemical Society 135 (2013) 17699–17702.
[17] C. Tsai, K. Chan, F. Abild-Pedersen, J.K. Nørskov, Active edge sites in $MoSe_2$ and WSe_2 catalysts for the hydrogen evolution reaction: A density functional study, Physical Chemistry Chemical Physics 16 (2014) 13156–13164.
[18] X.Q. Wang, Y.F. Chen, B.J.E. Zheng, F. Qi, J.R. He, P.J. Li, W.L. Zhang, Few-layered WSe_2 nanoflowers anchored on graphene nanosheets: A highly efficient and stable electrocatalyst for hydrogen evolution, Electrochimica Acta 222 (2016) 1293–1299.
[19] W.J. Zhou, K. Zhou, D.M. Hou, X.J. Liu, G.Q. Li, Y.H. Sang, H. Liu, L.G. Li, S.W. Chen, Three-dimensional hierarchical frameworks based on MoS_2 nanosheets self-assembled on graphene oxide for efficient electrocatalytic hydrogen evolution, ACS Applied Materials & Interfaces 6 (2014) 21534–21540.
[20] L.J. Yang, W.J. Zhou, D.M. Hou, K. Zhou, G.Q. Li, Z.H. Tang, L.G. Li, S.W. Chen, Porous metallic MoO_2-supported MoS_2 nanosheets for enhanced electrocatalytic activity in the hydrogen evolution reaction, Nanoscale 7 (2015) 5203–5208.
[21] H. Vrubel, X.L. Hu, Growth and activation of an amorphous molybdenum sulfide hydrogen evolving catalyst, ACS Catalysis 3 (2013) 2002–2011.
[22] H. Wang, Z. Lu, D. Kong, J. Sun, T.M. Hymel, Y. Cui, Electrochemical tuning of MoS_2 nanoparticles on three-dimensional substrate for efficient hydrogen evolution, ACS Nano 8 (2014) 4940–4947.
[23] Y.P. Li, Y.F. Yu, Y.F. Huang, R.A. Nielsen, W.A. Goddard, Y. Li, L.Y. Cao, Engineering the composition and crystallinity of molybdenum sulfide for high-performance electrocatalytic hydrogen evolution, ACS Catalysis 5 (2015) 448–455.
[24] B. Ni, X. Wang, Face the Edges: Catalytic active sites of nanomaterials, Advanced Science 2 (2015) 150085.
[25] Y. Yang, H.L. Fei, G.D. Ruan, C.S. Xiang, J.M. Tour, Edge-oriented MoS_2 nanoporous films as flexible electrodes for hydrogen evolution reactions and supercapacitor devices, Advanced Materials 26 (2014) 8163–8168.
[26] J. Xie, H. Zhang, S. Li, R. Wang, X. Sun, M. Zhou, J. Zhou, X.W.D. Lou, Y. Xie, Defect-rich MoS_2 ultrathin nanosheets with additional active edge sites for enhanced electrocatalytic hydrogen evolution, Advanced Materials 25 (2013) 5807–5813.
[27] D.Y. Chung, S.K. Park, Y.H. Chung, S.H. Yu, D.H. Lim, N. Jung, H.C. Ham, H.Y. Park, Y. Piao, S.J. Yoo, Y.E. Sung, Edge-exposed MoS_2 nano-assembled structures as efficient electrocatalysts for hydrogen evolution reaction, Nanoscale 6 (2014) 2131–2136.
[28] S.-K. Park, D.Y. Chung, D. Ko, Y.-E. Sung, Y. Piao, Three-dimensional carbon foam/N-doped graphene@MoS_2 hybrid nanostructures as effective electrocatalysts for the hydrogen evolution reaction, Journal of Materials Chemistry A 4 (2016) 12720–12725.
[29] X. Zhou, L.J. Wan, Y.G. Guo, Synthesis of MoS_2 nanosheet-graphene nanosheet hybrid materials for stable lithium storage, Chemical Communications 49 (2013) 1838–1840.
[30] S. Chen, J. Duan, Y. Tang, B. Jin, S.Z. Qiao, Molybdenum sulfide clusters-nitrogen-doped graphene hybrid hydrogel film as an efficient three-dimensional hydrogen evolution electrocatalyst, Nano Energy 11 (2015) 11–18.
[31] Y. Li, H. Wang, L. Xie, Y. Liang, G. Hong, H. Dai, MoS_2 nanoparticles grown on graphene: an advanced catalyst for the hydrogen evolution reaction, Journal of the American Chemical Society 133 (2011) 7296–7299.
[32] S. Reddy, R. Du, L.X. Kang, N.N. Mao, J. Zhang, Three dimensional CNTs aerogel/MoS_x as an electrocatalyst for hydrogen evolution reaction, Applied Catalysis B: Environmental 194 (2016) 16–21.
[33] H.H. Gu, Y.P. Huang, L.Z. Zuo, W. Fan, T.X. Liu, Graphene sheets wrapped carbon nanofibers as a highly conductive three-dimensional framework for perpendicularly anchoring of MoS_2: Advanced electrocatalysts for hydrogen evolution reaction, Electrochimica Acta 219 (2016) 604–613.
[34] L. Chen, C. Xu, R. Du, Y. Mao, C. Xue, L. Chen, L. Qu, J. Zhang, T. Yi, Rational design of three-dimensional nitrogen-doped carbon nanoleaf networks for high-performance oxygen reduction, Journal of Materials Chemistry A 3 (2015) 5617–5627.
[35] Y.F. Zhang, L.Z. Zuo, Y.P. Huang, L.S. Zhang, F.L. Lai, W. Fan, T.X. Liu, In-situ growth of few-layered MoS_2 nanosheets on highly porous carbon aerogel as advanced electrocatalysts for hydrogen evolution reaction, ACS Sustainable Chemistry & Engineering 3 (2015) 3140–3148.
[36] L. Liao, J. Zhu, X. Bian, L. Zhu, M.D. Scanlon, H.H. Girault, B. Liu, MoS_2 formed on mesoporous graphene as a highly active catalyst for hydrogen evolution, Advanced Functional Materials 23 (2013) 5326–5333.
[37] Y.F. Zhao, X.Q. Xie, J.Q. Zhang, H. Liu, H.J. Ahn, K.N. Sun, G.X. Wang, MoS_2 nanosheets supported on 3D graphene aerogel as a highly efficient catalyst for hydrogen Evolution, Chemistry-A European Journal 21 (2015) 15908–15913.
[38] L.Z. Zuo, W. Fan, Y.F. Zhang, L.S. Zhang, W. Gao, Y.P. Huang, T.X. Liu, Graphene/montmorillonite hybrid synergistically reinforced polyimide composite aerogels with enhanced flame-retardant performance, Composites Science and Technology 139 (2017) 57–63.
[39] Y. Wang, D.Z. Kong, W.H. Shi, B. Liu, G.J. Sim, Q. Ge, H.Y. Yang, Ice templated free-standing hierarchically WS_2/CNT-rGO aerogel for high-performance rechargeable lithium and sodium ion batteries, Advanced Energy Materials 6 (2016) 1301875.
[40] J.R. He, Y.F. Chen, W.G. Lv, K.C. Wen, C. Xu, W.L. Zhang, W. Qin, W.D. He, Three-dimensional CNT/graphene-Li_2S aerogel as freestanding cathode for high-performance Li-S batteries, ACS Energy Letters 1 (2016) 820–826.
[41] A.L. Higginbotham, D.V. Kosynkin, A. Sinitskii, Z. Sun, J.M. Tour, Lower-defect graphene oxide nanoribbons from multiwalled carbon nanotubes, ACS Nano 4 (2010) 2059–2069.
[42] L.Y. Jiao, L. Zhang, X.R. Wang, G. Diankov, H.J. Dai, Narrow graphene nanoribbons from carbon nanotubes, Nature 458 (2009) 877–880.
[43] W.S. Hummers, R.E. Offeman, Preparation of graphitic oxide, Journal of the American Chemical Society 80 (1958) 1339.
[44] A.L. Higginbotham, D.V. Kosynkin, A. Sinitskii, Z.Z. Sun, J.M. Tour, Lower-defect graphene oxide nanoribbons from multiwalled carbon nanotubes, ACS Nano 4 (2010) 2059–2069.